1 **Replication timing maintains the global epigenetic state in human cells**.

2

3 Kyle N. Klein[1,#], Peiyao A. Zhao[1,#], Xiaowen Lyu[2,#], Daniel A. Bartlett[1], Amar Singh[3], Ipek Tasan[4],

4 Lotte P. Watts[5], Shin-ichiro Hiraga[5], Toyoaki Natsume[6], Xuemeng Zhou[7], Danny Leung[7], Masato

5 T. Kanemaki[6], Anne D. Donaldson[5], Huimin Zhao[4], Stephen Dalton[3], Victor G. Corces[2], David M.

6 Gilbert[1,*].

7

8 [1]Department of Biological Science, 319 Stadium Drive, Florida State University, Tallahassee, FL

9 32306, USA.

10 [2]Department of Human Genetics, Emory University School of Medicine, Atlanta, GA 30322, USA

11 [3]Department of Biochemistry and Molecular Biology, University of Georgia, Athens, GA 30602,

12 USA.

13 [4]Department of Biochemistry, University of Illinois at Urbana-Champaign, Urbana, IL 61801,

14 USA.

15 [5]Institute of Medical Sciences, University of Aberdeen, Aberdeen, AB25 2ZD, UK.

16 [6]Department of Chromosome Science, National Institute of Genetics, Research Organization of

17 Information and Systems (ROIS), Yata 1111, Mishima, Shizuoka 411-8540, Japan. Department

18 of Genetics, The Graduate University for Advanced Studies (SOKENDAI), Yata 1111, Mishima,

19 Shizuoka 411-8540, Japan

20 [7]Divison of Life Science, Hong Kong University of Science and Technology, Clear Water Bay,

21 Hong Kong, China

22 # These authors contributed equally

23 *Correspondence to: gilbert@bio.fsu.edu

24

25 **Abstract:**

26

27 DNA is replicated in a defined temporal order termed the replication timing (RT) program. RT is

28 spatially segregated in the nucleus with early/late replication corresponding to Hi-C A/B

29 chromatin compartments, respectively. Early replication is also associated with active histone

30 modifications and transcriptional permissiveness. However, the mechanistic interplay between

31 RT, chromatin state, and genome compartmentalization is largely unknown. Here we report that

32 RT is central to epigenome maintenance and compartmentalization in both human embryonic

33 stem cells (hESCs) and cancer cell line HCT116. Knockout (KO) of the conserved RT control

34 factor RIF1, rather than causing discrete RT switches as previously suspected, lead to

35 dramatically increased cell to cell heterogeneity of RT genome wide, despite RIF1's enrichment

36 in late replicating chromatin. RIF1 KO hESCs have a nearly random RT program, unlike all prior

37 RIF1 KO cells, including HCT116, which show localized alterations. Regions that retain RT,

38 which are prevalent in HCT116 but rare in hESCs, consist of large H3K9me3 domains revealing

39 two independent mechanisms of RT regulation that are used to different extents in different cell

40 types. RIF1 KO results in a striking genome wide downregulation of H3K27ac peaks and

41 enrichment of H3K9me3 at large domains that remain late replicating, while H3K27me3 and

42 H3K4me3 are re-distributed genome wide in a cell type specific manner. These histone

43 modification changes coincided with global reorganization of genome compartments,

44 transcription changes and a genome wide strengthening of TAD structures. Inducible

45 degradation of RIF1 revealed that disruption of RT is upstream of genome compartmentalization

46 changes. Our findings demonstrate that disruption of RT leads to widespread epigenetic mis-

47 regulation, supporting previously speculative models in which the timing of chromatin assembly

48 at the replication fork plays a key role in maintaining the global epigenetic state, which in turn

49 drives genome architecture.

50

51 **Main Text:**

52

53 DNA is replicated during S phase of the cell cycle in a temporal order known as the replication

54 timing (RT) program. RT is conserved among eukaryotes, cell type specific and correlates with

55 many important epigenomic features (*1*). Early replicating chromatin has euchromatic

56 characteristics such as active histone modifications and location in the nuclear interior while late

57 replicating chromatin is associated with heterochromatic features like transcriptionally

58 repressive histone modifications and location at the nuclear periphery. Early and late replicating

59 chromatin correspond to A- and B-compartments respectively as defined by high throughput

60 chromatin conformation capture (Hi-C) (*2*). Despite these close correlations, the mechanistic link

61 between RT and the accurate maintenance of chromatin through cell cycles remains elusive.

62 Prior work has shown that histones and their modifications are both recycled from parental

63 chromatin and added and modified de novo after passage of the replication fork with different

64 chromatin states showing differing dynamics of reassembly (*3, 4*). It has long been

65 hypothesized that RT influences chromatin maintenance. Indeed, microinjection of plasmids into

66 mammalian nuclei revealed that plasmids replicated in early S phase were decorated with

67 acetylated histones, while those replicated later in S phase were devoid of acetylated histones

68 (*5*). However, there is still no direct evidence implicating RT in epigenetic state maintenance,

69 largely due to the inability to manipulate genome wide RT. Recently the conserved protein RIF1

70 has been shown to affect RT in many eukaryotes, however, partly because the effects have

71 been partial or localized, RIF1 disruption has not been exploited to study the effects of RT

72 abrogation (*6–11*).

73

74 To gain insight into the role of genome wide RT as controlled by RIF1 in shaping the epigenome

75 we examined the effects of RIF1 knock out (KO) in three human cell lines. H9 hESC, HCT116,

76 established by removal of RIF1 exon 3 (Fig. S1a, b, c). As previously reported (*11*), RIF1 KO

77 cells proceeded through the cell cycle with minor decreases in the number of S phase cells and

78 increases in the number of gap phase cells (Fig S1d, e). All three RIF1 KO cell lines exhibit

79 genome wide aberrations in RT measured using E/L Repli-seq (*12*) but with varying degrees of

80 severity (Fig. 1a). Similar to all prior reports in mammalian cells (*8, 9, 11*), discrete domains

81 changed RT either from early to late (EtL) or late to early (LtE) in E/L RT profiles of HCT116 and

82 HAP1 cells. RIF1 KO caused 43% of the genome to change RT (23% EtL and 20% LtE) in

83 HCT116 and HAP1 cells. However, in H9 hESCs (Fig. 1a), nearly the entire genome acquired a

84 log2E/L dynamic range close to zero (Fig 1b), precluding identification of specific domain level

85 RT changes and suggesting that RIF1 is necessary for nearly all temporal control of replication

86 in hESCs. This near complete loss of RT control in RIF1 KO hESCs was much more severe

87 than we previously reported in RIF1 KO mouse ESCs (*11*) (Fig S1f). Moreover, partial

88 knockdown (KD) of RIF1 in H9 hESCs using an shRNA (Fig S2a) resulted in a partial effect on

89 the RT program (Fig S2b), demonstrating that RIF1's control of global RT in hESCs is dosage

90 dependent. Plotting the density of RT values as a histogram confirmed that all three RIF1 KO

91 cell lines, as well as RIF1 KD H9 hESCs, show genome wide RT values accumulating near the

92 middle of S phase for most genomic bins (Fig 1b, Fig S2c) and that H9 RIF1 KO cells showed a

93 sharp genome wide peak of log2E/L values at zero (Fig 1b). Replication foci patterns assayed

94 by BrdU incorporation, which track with genome wide RT (*13*) (Fig S3a), were also altered (Fig

95 S3b) as RIF1 KO cells showed a loss of clear middle S phase patterns and 'blending' of early

96 and middle replication foci patterns but maintained distinct early and late foci patterns (Fig S3a,

97 b). Together, these results demonstrate a considerably more extensive role for RIF1 in RT

98 control in hESCs than in any other mammalian cell type so far studied.

99

100 Previous reports have interpreted RT changes in RIF1 KO cells as distinct RT switches (*8, 9,*

101 *11*) but the extent of the RT phenotype in RIF1 KO hESCs made us hypothesize that RIF1 KO

102 results in a loss of temporal replication specificity resulting from increased cell to cell RT

103 heterogeneity within the population. To address this hypothesis, we applied our recently
104 developed high resolution Repli-seq protocol (*14*), which uses a shorter nascent DNA labelling
105 period and divides S phase into 16 small, evenly distributed fractions. High resolution Repli-seq
106 produces RT heatmaps that capture peaks of replication initiation termed initiation zones (IZs)
107 and large valleys of late replication that are sites of termination containing broadly distributed,
108 low efficiency initiation events (*14*). Distinct changes in RT, such as those that occur during
109 stem cell differentiation, manifest as clear EtL or LtE shifts of peaks and valleys on the temporal
110 axis (*14*), whereas greater RT variation would manifest as highly diffused peaks or valleys
111 resulting from reads spread out across many S phase fractions for any genomic location. High
112 resolution Repli-seq of RIF1 KO cells revealed dramatic diffusion of RT patterns and loss of
113 defined IZs in both HCT116 and H9 hESCs (Fig 1c, Fig S4a, b) indicating major RT variation
114 within the cell population. EtL and LtE regions in RIF1 KO HCT116 cells called in E/L Repli-seq
115 showed major loss of temporal control and replication across a broad distribution of times during
116 S phase in the high resolution Repli-seq (Fig S4c). Surprisingly, even early replicating regions
117 that were not called as statistically confident EtL switches in the HCT116 E/L Repli-seq also lost
118 definition of IZs and RT control when assayed using the more sensitive high resolution Repli-
119 seq (Compare Figs. 1a, c, Fig S4c). Thus, the entirety of the early replicating genome lost RT
120 control upon RIF1 KO in both cell lines. By contrast, many late replicating regions in HCT116
121 not called as LtE switches in E/L Repli-seq retained late replication control when assayed by
122 high resolution Repli-seq (Fig S4c) indicating a separate, RIF1-independent mechanism
123 controlling RT for these late regions in HCT116, which we will expand upon below. Remarkably,
124 high resolution Repli-seq of RIF1 KO H9 hESCs resulted in a heatmap that lacked distinct IZs
125 and valleys, suggesting a near complete genome-wide loss of temporal replication control in
126 which any sequence can replication at any time in the cell population (Fig 1d).

127

128 To better quantify the extent and temporal direction of the loss of RT control, we calculated RT
129 indices for all genomic bins of high resolution Repli-seq in WT and RIF1 KO samples where
130 positive values indicate early replication and negative values indicate late replication (Fig S4d,
131 Methods). Again, early replicating regions that were not called as EtL switches in the HCT116
132 E/L Repli-seq showed noticeable changes in their RT indices similar to called EtL switches (Fig
133 S4e). RT differences (RT_{diff}) were then calculated by subtracting RIF1 KO RT indices from WT
134 RT indices (Methods). We further applied a 3 component Gaussian Mixture model to RT_{diff}
135 distribution to identify genomic bins that were characterized by: 1) negative RT_{diff}, which are
136 regions that are later replicating in WT and earlier replicating in KO, 2) positive RT_{diff}, which are

137   regions that are earlier replicating in WT and later replicating in KO, 3) close-to-zero RT_{diff}, which

138   are regions that showed limited RT difference between WT and KO or could not be called as

139   significantly different (Fig S4f, Methods). 86% and 78% of the genome showed significant RT_{diff}

140   in H9 and HCT116, respectively (Fig S4f table). These results demonstrate a much more

141   significant effect of RIF1 loss on RT in both cell types than previously imagined.

142

143   To examine the effect of RIF1 deletion on replication initiation within IZs genome wide, we

144   divided each IZ called in high resolution WT Repli-seq data into timing categories based on the

145   temporal position of the IZ peak in S phase (*14*) and plotted the cumulative percentage of DNA

146   replicated through S phase in both WT and RIF1 KO cells (Fig 1d). WT cells showed typical

147   segregation of IZs according to the temporal order associated with steady state replication and

148   steep sigmoidal-like curves (*14*) while RIF1 KO cells showed major overlap of IZ classes and

149   flatter sigmoidal-like curves (Fig 1d) showing that RIF1 KO caused loss of genome wide

150   replication initiation timing specificity in both cell lines, with H9 hESCs losing any detectable

151   temporal control. To quantify this change we calculated the parameter T_{width} as the time between

152   when 25% and 75% of cells replicate for each genomic bin. A small T_{width} is indicative of a more

153   deterministic replication scheme whereas a larger T_{width} is representative of greater heterogeneity.

154   Genome wide measurement of T_{width} greatly increased in both cell types upon RIF1 KO indicating

155   a major increase in RT heterogeneity (Fig S4g).

156

157   To directly validate that the RT aberration seen in RIF1 KO was due to increased cell to cell RT

158   heterogeneity we performed our recently developed single-cell Repli-seq (*15*) on human haploid

159   HAP1 WT and RIF1 KO cells, which eliminate allelic RT variation to enable single cell analysis.

160   RIF1 KO caused a major increase in RT heterogeneity genome wide, confirming this effect in a

161   third cell line. We ranked binarized single cell RT profiles by their percentage of genome

162   replicated indicating their progression through S phase and constructed heatmaps representing

163   replicated or unreplicated windows for WT and RIF1 KO cells (Fig 1e). WT heatmaps

164   correspond well to E/L Repli-seq, early replicating regions manifested as distinct domains that

165   have finished replication early in S phase in the majority of cells whereas late replicating regions

166   remained unreplicated until the later stages of S phase (Fig 1e). In KO heatmaps, however, the

167   distinction between early and late replicating domains was blurred at all stages of S phase (Fig

168   1e, Fig S4h). To quantify this heterogeneity genome wide we assumed a 10 hour S phase and

169   calculated 'time from population average replication according to E/L RT values' at 0.1 intervals

170   for each single cell (*15*) and plotted the relationship between percentage of genomic bins

171   replicated to their 'time from population average replication' in the form of heatmaps (Fig 1f). We

172   then performed sigmoidal fitting on the heatmap and calculated the parameter T_{width} for each bin

173   (See Methods). HAP1 WT cells' T_{width} was 3.9 hours while the absence of RIF1 greatly increased

174   the T_{width} to 8.4 hours indicating a major increase in RT heterogeneity (Fig 1f). Taken together,

175   both high resolution Repli-seq and single cell Repli-seq demonstrate that loss of RIF1 in 3

176   human cell lines disrupts RT by dramatically increasing temporal heterogeneity of replication

177   across the cell population rather than causing discrete RT shifts in all cells.

178

179   Mouse RIF1 was previously reported to bind late replicating chromatin (*11*). We performed

180   Cut&Run (*16*) against GFP on GFP tagged RIF1 in HCT116 and H9 hESCs (Fig S1a, b) to map

181   RIF1 binding in human cells. Consistent with mESCs (*11*), RIF1 binding was enriched in the late

182   replicating portion of the genome in both cell lines (Fig S5a) and bound chromatin in broad

183   domains rather than distinct peaks (Fig 2a). We first divided the late replicating genome into

184   regions that lost RT control upon RIF1 KO, characterized by continuous bins displaying negative

185   RT_{diff} (Fig 2b blue in WT, red in KO) and those that maintained their late RT upon RIF1 KO,

186   characterized by continuous bins displaying close-to-zero RT_{diff} (Fig 2d blue in WT, blue in KO).

187   These regions are hereafter referred to as 'affected' or 'unaffected' late regions respectively (Fig

188   2a, b, c, d). RIF1 binding was especially enriched at affected domains (Fig 2a, e) while

189   unaffected domains showed lower RIF1 enrichment in both cell lines (Fig 2c, e). Contrary to

190   what was reported in mESCs (*11*), unaffected regions showed no preferential association with

191   the nuclear lamina than affected regions via Lamin B1 DamID (Fig 2b, c).

192

193   To further investigate these late replicating regions, we performed ChIP-seq on the late

194   replication associated marks H3K9me3 and H3K27me3 in both HCT116 and H9 hESC RIF1 KO

195   cells. H3K9me3 marked regions manifest as either small peaks or large megabase scale

196   domains (*17*). In WT cells, affected regions were enriched for smaller H3K9me3 peaks while

197   unaffected regions contained larger H3K9me3 domains (Fig 2a, c, e, Fig S5b). RIF1 KO caused

198   genome wide changes to H3K9me3 peaks and domains in both cell lines (Fig S5c). Without

199   RIF1, small H3K9me3 peaks were lost, coincident with a loss in RT control (Fig 2a, c, e).

200   However, the large H3K9me3 domains, which are far more abundant in HCT116 than H9

201   hESCs, dramatically increased in their density of H3K9me3 and retained their late RT in the

202   absence of RIF1 (Fig 2c, e). In fact, almost all regions that retained late RT in RIF1 KO HCT116

203   cells (n=209) were large H3K9me3 domains. The rare domains that retained late RT in H9

204   hESCs (n=49) were also large H3K9me3 domains. Overall levels of H3K9me3 within RIF1 KO

205 H9 hESCs did not change compared to WT (Fig S5d) suggesting that total H3K9me3 is
206 redistributed rather than gained or lost upon RIF1 KO. Most H3K9me3 unaffected regions do
207 not overlap between cell types, consistent with the model that these H3K9me3 domains are
208 developmentally regulated and implicated in silencing of lineage inappropriate genes (*17*) (Fig
209 S5e). By contrast, H3K27me3 changes after RIF1 KO were cell type specific (Fig 2a, c, e).
210 H3K27me3 peaks were enriched at affected regions but depleted from unaffected regions in WT
211 HCT116 cells and these distributions were unaffected by RIF1 KO (Fig 2a, c, e). However,
212 H3K27me3 was similar to H3K9me3 in H9 hESCs in that RIF1 loss resulted in the depletion of
213 H3K27me3 peaks at affected regions and enrichment at the few unaffected regions (Fig 2a, c,
214 e). Thus, RIF1 and H3K9me3 domains are two separate mechanisms that orchestrate late RT
215 to different extents in different cell types.
216
217 The strong association between late replication and B compartmentalization as defined by
218 negative PC1 Eigenvector values (*18*, *19*) compelled us to investigate the genomic
219 compartmentalization and architecture of RIF1 KO cells by Hi-C (*20*). Surprisingly, we found that
220 affected and unaffected regions, despite being similarly late replicating, have distinct
221 compartmental identities. In WT cells unaffected regions were associated with more negative
222 PC1 Eigenvector values and thus interacted more strongly with other B compartment regions
223 than affected regions (Fig 2f), while affected regions showed a slight interaction preference to
224 the A compartment particularly in HCT116 cells (Fig 2f). Upon RIF1 KO, the interaction between
225 unaffected regions with the rest of the B compartment was strengthened whereas affected
226 regions display more preferential interactions with the A compartment (Fig 2f) indicating RIF1
227 delays the replication of regions in A compartment that would otherwise be earlier replicating.
228 Moreover, WT interactions between unaffected regions were significantly stronger than
229 interactions between affected regions or interactions between unaffected regions and affected
230 regions (Fig 2g) further confirming that affected and unaffected regions are two intrinsically
231 different classes of late replicating regions with distinct interaction preferences. These distinct
232 interaction preferences further increase in RIF1 KO (Fig 2g). We next looked to see if RIF1 KO
233 had an effect on the distribution of histone marks between genomic compartments by plotting
234 the aggregate log2 fold enrichment of histone modification ChIP-seq centered at the A/B
235 compartment boundary (Fig 2h). H3K9me3 was depleted from the A compartment and enriched
236 in the B compartment in HCT116 RIF1 KO cells (Fig 2h) consistent with the fact that in HCT116
237 affected regions were more associated with the A compartment while unaffected regions were
238 predominately within the B compartment (Fig 2f). Similarly, RIF1 KO H9 hESCs had depleted

239   H3K9me3 in the A compartment, however the B compartment as a whole also lost H3K9me3

240   (Fig 2h) as the majority of B compartment regions were affected and lost late replication

241   specificity. H3K27me3 changes were cell type specific as distributions remained largely

242   unchanged in HCT116 but showed a decrease in both compartments in H9 hESCs (Fig 2h).

243   These data indicate RT affected and unaffected regions are two distinct classes of late

244   replicating chromatin which are differentially affected by RIF1 KO.

245

246   New interactions evident in Hi-C contact maps were formed between unaffected regions that

247   became highly enriched for H3K9me3 in RIF1 KO cells (Fig 2i). Interactions between H3K9me3

248   peaks were strengthened after RIF1 KO and driven by enriched H3K9me3 domains in

249   unaffected regions (Fig S5f, g). We further sorted and binned intra B-compartment interactions

250   according to the extent of H3K9me3 peak changes (negative: downregulated, positive:

251   upregulated). In WT cells upregulated H3K9me3 domains and downregulated H3K9me3 peaks

252   form separate interaction hubs within the B compartment (Fig 2j left). Interactions within these

253   hubs, particularly the upregulated H3K9me3 domains, strengthen dramatically upon RIF1 KO

254   (Fig 2j right). These results demonstrate that H3K9me3 domains form strong interactions with

255   one another constituting one type of B compartment that maintains its late RT and strengthens

256   its interactions without RIF1 whereas regions that lack large H3K9me3 domains form a separate

257   hub of interactions and require RIF1 to enforce late replication.

258

259   RIF1 KO and subsequent loss of global RT not only caused substantial changes in B

260   compartment associated chromatin modifications and interactions, but it also had a genome-

261   wide effect on A compartment associated chromatin modifications. ChIP-seq on H3K27ac and

262   H3K4me3 revealed a genome wide reduction of H3K27ac peaks (Fig S5h) along with specific

263   changes in H3K4me3 in RIF1 KO cells. Similar to H3K9me3, RIF1 KO did not cause a change

264   in global levels of H3K27ac in H9 hESCs compared to WT (Fig S5i) again suggesting

265   redistribution rather than global reduction of chromatin marks upon RIF1 KO. H3K27ac and

266   H3K4me3 became majorly depleted in the A compartment of both cell lines with mild increases

267   in their association with the B compartment (Fig 3a). Loss of active marks from the A

268   compartment, particularly H3K27ac, was concurrent with changes in compartmentalization and

269   Hi-C contacts in both cell lines. In H9 hESCs the majority of compartment changes were the

270   disappearance of small A compartments into neighboring B compartments (Fig 3b, c), while

271   HCT116 exhibited discrete shifts in compartmentalization in both directions from A to B as well

272   as B to A (Fig 3b). In both cell lines the compartmental switches lead to a more consolidated

273   appearance in the correlation matrix heatmap (Fig 3b). Loss of A compartment interactions in

274   Hi-C contact maps corresponded to reduced H3K27ac peaks in both cell lines (Fig 3c (arrows)).

275   Within all A to B compartment switches genome wide the level of H3K27ac was majorly

276   depleted in both cell lines (Fig 3d). Genome-wide interaction pileups showed specific

277   interactions between H3K27ac peaks and all other H3K27ac peaks were drastically reduced at

278   A to B compartment switches (Fig 3e). Changes in genome organization were not due to

279   changes in cell cycle distributions as RIF1 KD H9 hESCs exhibited similar changes to cell cycle

280   as KO (Fig S1d, e) without changes in genome organization (Fig S2d, e, f). These data strongly

281   suggest that depletion of active histone modifications, particularly H3K27ac, leads to loss of A

282   compartment interactions in RIF1 KO cells.

283

284   Both cell lines exhibited genome wide weakening of A/A interactions accompanied by

285   strengthening of B/B interactions (Fig 3f). This was further confirmed when we called statistically

286   significant differential interactions (strengthened and weakened) using diffHiC (*21*).

287   Strengthened interactions were seen predominantly within the B compartment and weakened

288   interactions were concentrated in the A compartment in both cell lines (Fig S6a, b). This is likely

289   the combined effect of strengthened interactions between upregulated H3K9me3 domains

290   within the B compartment (Fig S5f, g) and weakened interactions between downregulated

291   H3K27ac peaks in the A compartment (Fig 3e). Together these data indicate a substantial

292   reorganization of compartments in accordance with epigenome changes in RIF1 KO cells.

293

294   TAD boundaries, called by directionality index (DI) (*22*), also changed locally in conjunction with

295   shifts in RT and epigenetic state. In individual cases where a large late replicating domain broke

296   into an unaffected region and an affected region upon RIF1 KO, a new TAD boundary formed in

297   accordance with the new RT boundary demarcated by enriched H3K9me3 showing that

298   changes in chromatin state correlated with loss of RT control can permit the formation of new

299   TAD boundaries (Fig S7a). New TAD boundaries were formed within affected late regions in

300   HCT116, consistent with their earlier RT indices and increased A-compartment association (Fig

301   S7b bottom, c) as early replicating, A compartment chromatin typically contains numerous TADs

302   while late, B compartment chromatin contains fewer TADs (*22*). Reciprocally, boundaries were

303   also lost in regions of later RT (Fig S7b top). Genome wide, the number (~4000 in H9 hESC and

304   ~2600 in HCT116) and positioning of TAD boundaries remained similar between WT and RIF1

305   KO (Fig S7d), while the strength of TAD boundaries was increased in RIF1 KO measured by

306   insulation score (Fig S7d, e, f). Consistently, the ratio of intra-TAD/inter-TAD interactions was

307   increased in RIF1 KO, particularly in HCT116, (Fig S7g) suggesting overall TAD strengthening.

308   ChIP-seq of the essential TAD protein cohesin's subunit Rad21 revealed largely unaffected

309   binding with a small number of up and down regulated peaks in both cell lines (Fig S8a).

310   Focusing on the interactions at common, up, and down regulated Rad21 peaks, we found that

311   boundaries were strengthened around common and up regulated peaks in both cell lines (Fig

312   S8b). In HCT116, boundaries were strengthened even around downregulated peaks (Fig S8b

313   left) suggesting changes in TAD boundaries were not due to changes in Rad21 peak intensity.

314   In H9 hESCs, we observed weakening of boundaries around the small number of

315   downregulated Rad21 peaks (Fig S8b right). However, such boundaries were weak boundaries

316   in WT and constituted a small fraction of total boundaries (Fig S8b right). Overall, these data

317   mechanistically separate RT from TAD formation and support previous work showing essential

318   TAD proteins Rad21 and CTCF are dispensable for global RT control (*23–25*).

319

320   To investigate if the profound changes in genome organization and epigenetic state seen in

321   RIF1 KO cells affected gene expression we performed RNA-seq on WT and RIF1 KO HCT116

322   and H9 hESCs. With the threshold for called change set at FDR < 0.1, RIF1 KO caused 2284

323   genes (1378 upregulated, 906 downregulated) in H9 hESCs and 1737 genes to change

324   expression (818 upregulated, 919 downregulated) in HCT116 (Fig S9a). Gene ontology (GO)

325   analysis revealed expression changes for genes important for cancer progression in HCT116

326   and developmentally regulated genes in H9 hESCs (Fig S9b). However, H9 hESCs devoid of

327   RIF1 did not have significantly reduced expression of Oct4, Nanog, Sox2, Rex1, or any other

328   key pluripotency factors (Fig S9c), consistent with their ability to self-renew (Fig S1c) with no

329   morphological signs of differentiation. RT and chromatin compartmentalization are correlated

330   with gene expression (*1*), however we observed no universal pattern linking changed gene

331   expression and changed RT or compartmentalization. Neither changes in RT nor compartment

332   switches were able to predict gene expression changes in RIF1 KO cells of either cell type (Fig

333   S9d, e). Loss of late timing was not correlated with increased gene expression nor was loss of

334   earlier timing correlated with decreased expression (Fig S9d). Similarly, shifts from the B to A

335   compartment were not correlated with increased gene expression nor were shifts from A to B

336   correlated with downregulated expression (Fig S9e). However, the WT chromatin context of

337   differentially expressed genes did correlate with expression changes. In H9 hESCs where the

338   epigenetic landscape is plastic (*26, 27*) earlier replicating genes with strong A compartment

339   association in WT cells were likely to be downregulated while later replicating genes with weak

340   A compartment association in WT cells were likely to be upregulated upon RIF1 KO (Fig S9d, f).

341   In HCT116 cells, only genes in early replicating, A compartment chromatin were differentially

342   expressed (both up and downregulated) and mostly maintained their early replication (albeit

343   more temporally heterogeneous) and A compartmentalization upon RIF1 KO (Fig S9d, e, f, g).

344   Conversely, specific chromatin modifications were more correlated to gene expression changes

345   upon RIF1 loss than changes in RT or 3D genomic organization. Differentially expressed genes

346   showed cell type specific changes in the distribution of specific histone modifications around

347   their TSSs that correlated with expression changes (Fig S9h). In H9 hESCs H3K27me3 was

348   high in WT cells around TSSs of upregulated genes and decreased upon RIF1 KO while levels

349   of H3K27me3 remained constantly low around downregulated genes (Fig S9h, left). WT

350   H3K9me3 levels were low around both up and downregulated genes and didn't change

351   significantly upon RIF1 KO (Fig S9h, left). Both up and downregulated TSSs showed similar

352   changes to the active marks that reflected the global trend of change. H3K27ac was diminished

353   and H3K4me3 remained largely constant (Fig S9h, left). Taken together, random forest

354   regression feature importance analysis showed H3K27me3 to be most important in predicting

355   gene expression changes in H9 hESCs (Fig S9i). As most genes that were differentially

356   expressed in HCT116 were associated with the A compartment and early replication in WT

357   cells, these TSSs showed changes in histone mark distribution similar to changes in the A

358   compartment as a whole (Fig 2j bottom, Fig 3a bottom). H3K27ac was diminished while

359   H3K27me3 levels remained constant at both up and down regulated genes (Fig S9h, right).

360   However, changes in H3K4me3 levels did correlate with expression changes (Fig S9h, right). In

361   summary, we found changes in histone modifications around the TSS were considerably more

362   predictive of gene expression changes than changes to RT and genome compartmentalization.

363

364   Temporal separation of the genome into early and late replicating chromatin is thought to help

365   coordinate chromatin states after the passage of the replication fork where early replicating

366   chromatin is likely to be assembled into open euchromatin while late replicating chromatin is

367   likely to be assembled into heterochromatin (5). However, there has been no evidence for this

368   on native mammalian chromosomes due to the prior inability to manipulate RT. We found that

369   loci depleted for H3K27ac were in genomic bins that became later replicating on the population

370   level as a result of RIF1 KO (Fig 3g top). Reciprocally, those few peaks that became more

371   enriched for H3K27ac in RIF1 KO were in bins that became earlier replicating (Fig 3g top). A

372   similar correlative change was seen at H3K9me3 peaks where loci that became depleted for

373   H3K9me3 became earlier replicating while enriched peaks became later replicating (Fig 3g

374   bottom). This correlation is consistent with the model that RT plays a role in establishing the

375   characteristics of nascent chromatin (*5*). Our observation that global histone modification levels

376   are not affected by RIF1 KO (Fig S5d, i) also supports this model as altered RT would predict

377   redistribution of chromatin modifications rather than global gain or loss of histone marks.

378   Furthermore, RIF1 KD in H9 hESCs showed mild disruptions to RT (Fig S2b, c), but no changes

379   in genome compartmentalization (Fig S2d, e, f) indicating that RIF1's primary role is to control

380   RT and disruptions to epigenetic state and genome architecture are downstream and manifest

381   only when RT disruption are severe.

382

383   To more directly address RIF1's primary mode of action we took advantage of the auxin

384   inducible degron (AID) system (*28*) in HCT116 cells to rapidly degrade GFP tagged RIF1. After

385   24 hours of RIF1 degradation (Fig 4a) constituting ~1 cell cycle the RT phenotype observed in

386   RIF1 KO HCT116 cells was fully recapitulated while changes to genome organization were not

387   as striking as RIF1 KO. Genome wide RT defects assayed by E/L Repli-seq (Fig 4b, c) showed

388   RT values centered around zero log2E/L and the retention of a subset of late replicating regions

389   in RIF1-AID cells similar to RIF1 KO (Fig 4b, c). However, RIF1-AID depleted cells showed few

390   compartmentalization switches (Fig 4d) and genome-wide intra- and inter- compartment

391   interactions were similar to RIF1-AID control cells (Fig 4e). Moreover, Euclidean distance

392   measurements between RIF1-AID depleted cells and either RIF1-AID control cells or RIF1 KO

393   cells showed genome wide RT values of RIF1-AID depleted cells were closer in Euclidean

394   distance and thus more similar to RIF1 KO cells. By contrast, genome wide Hi-C

395   log2(observed/expected) values of RIF1-AID depleted cells were more similar to RIF1-AID

396   control cells (Fig 4f). Furthermore, RIF1-AID depleted cells did not show increased interactions

397   between upregulated H3K9me3 domains called in RIF1 KO HCT116 cells (Fig 4g, h; compare

398   to Fig 2j and Fig S5d respectively) nor did these cells lose interaction between depleted

399   H3K27ac peaks called in RIF1 KO HCT116 cells (Fig 4i; compare to Fig 3e) suggesting that the

400   epigenetic chromatin state and thus genome compartmentalization are maintained after 24

401   hours of RIF1 depletion despite a nearly complete effect on RT. These data provide further

402   evidence that RIF1's primary role is to control RT and suggest that several cell cycles of

403   severely   disrupted   genome   wide   RT   is   required   to   significantly   affect   genome

404   compartmentalization, placing altered RT upstream of the other changes.

405

406   In conclusion, we have shown that late replicating genome is composed of two types of

407   domains, whose delayed replication is enforced by either H3K9me3 or RIF1. The two types of

408   domains form separate hubs of B compartment interactions. Deletion of RIF1 results in genome

409   wide RT disruption resulting from an increase in cell to cell heterogeneity of replication initiation

410   rather than discrete changes in RT. In both hESCs and HCT116 cells, RIF1 KO leads to

411   widespread aberrant histone modification patterns which correlate with distinct genome-wide

412   changes in 3D genome architecture and gene expression. We further show that RT abrogation

413   precedes changes in compartmentalization. We propose that RT changes due to RIF1 KO

414   results in aberrant re-establishment of epigenetic marks at replication forks that causes

415   profound changes in the epigenetic landscape that then alter genome architecture (Fig 4j) rather

416   than RIF1 acting directly to control genome organization as has been previously proposed (*11*).

417   We also show that despite massive epigenetic de-regulation, cells proliferate nearly normally.

418   Since Rif1 KO mice die in utero after gastrulation (*29*), we speculate that RIF1 is needed to

419   coordinate epigenetic changes during cell fate transitions but it, and the proper regulation of

420   epigenetic state, is dispensable for basic cell growth and proliferation. Further exploration of the

421   effects of RIF1 KO on lineage commitment in hESCs us thus poised to unveil insights into the

422   role of epigenetic stability in early human development. Our work establishes RIF1 as a key

423   regulator of epigenome maintenance through its role in RT establishment. Our experiments

424   exploit this role of RIF1 to provide the first mechanistic evidence linking the RT program with

425   maintenance of the global epigenetic state.

426

427   **Figure Legends:**

428

429   **Figure 1. RIF1 controls RT by reducing cell to cell variation in replication timing.**

430   a, E/L Repli-seq plots of Chr1 172.6-197.6 Mb in WT and two RIF1 KO clones overlaid in H9

431   hESCs (top) and HCT116 (middle) and HAP1 (bottom) cell lines. b, Genome wide probability

432   density of E/L RT values in H9 hESCs (left), HCT116 (middle), and HAP1 (right) WT (black) and

433   RIF1 KO (blue and red). c, High resolution Repli-seq plots of Chr1 172.6-197.6 Mb in WT and

434   RIF1 KO in H9 hESCs (top two) and HCT116 (bottom two); same locus as a. d, Cumulative

435   percent-replicated plots for each IZ called in WT cells versus S phase fraction of 16 fraction

436   Repli-seq color coded by their timing (red: early, blue: early mid, green: late mid, black: late). e,

437   Binarized single-cell Repli-seq heatmaps of Chr4 in HAP1 WT (top) and RIF1 KO (bottom)

438   sorted by percentage replicated where the top row represents the cell with the lowest

439   percentage of genome replicated and the last row represents the cell with the most percentage

440   of genome replicated. f, Sigmoidal fitting of the percentage replicated against time in hours from

441   population average replication for HAP1 WT (left) and RIF1 KO (right). The heatmaps (blue for

442   WT and red for KO) represent the data spread of percentage replicated (y-axis) against time

443   from population average replication (x-axis) for all 50kb bins genome wide for all cells. Dotted

444   lines at 25% of cells replicated and 75% of cells replicated indicate the span of T_{width}.

445

446   **Figure 2. RT affected and unaffected regions are distinct classes of chromatin.**

447   a, Affected region at Chr1 94.3-101.6 Mb in HCT116 (left) and Chr1 66.75-71.4 Mb in H9

448   hESCs (right) showing from top to bottom: 16 fraction Repli-seq in WT and RIF1 KO cells, RIF1

449   Cut&Run in WT cells, Lamin B1 DamID in WT cells, H3K9me3 ChIP-seq in WT and RIF1 KO

450   cells, and H3K27me3 ChIP-seq in WT and RIF1 KO cells. b, Heat maps of RT indices for

451   affected regions in WT and RIF1 KO of HCT116 and H9 hESCs. c, Unaffected region at Chr9

452   113.95-122.3 Mb in HCT116 (left) and Chr1 151.7-153.75 Mb in H9 hESCs (right) showing the

453   same panels as a. d, Heat maps of RT indices for unaffected regions in WT and RIF1 KO of

454   HCT116 and H9 hESCs. e, Fold enrichment signal pile ups of signal from indicated assay in

455   HCT116 (left) and H9 hESC (right) WT or RIF1 KO cells centered on affected regions (top) or

456   unaffected regions (bottom) ±4 Mb and sorted by size. Line plots represent cumulative signal in

457   WT (black) and RIF1 KO cells (blue). f, Violin plots of PC1 Eigenvector values for LtE and

458   unaffected chromatin loci in WT and RIF1 KO HCT116 (left) and H9 hESCs (right); (***p <

459   0.0005, **p < 0.005). g, Box plots of interaction strength between and within LtE and unaffected

460   chromatin domains in WT and RIF1 KO HCT116 (left) and H9 hESCs (right); (***p < 0.0005, **p

461   < 0.005). h, Pile up line plots of indicated histone marks at A to B compartment boundary ±1 Mb

462   in WT (black) and RIF1 KO (blue) HCT116 and H9 hESCs. i, H9K9e3 ChIP-seq tracks beside

463   ICE normalized Hi-C contact maps of HCT116 WT and RIF1 KO. j, Log2(obs/exp) aggregate

464   interactions between B compartments in WT and RIF1 KO HCT116 (top) and H9 hESCs

465   (bottom), The interactions were binned into 11 equal segments, which were ranked by

466   increasing delta H3K9me3 within B compartments where negative and positive values indicate

467   decrease and increase in H3K9me3 between WT and RIF1KO.

468

469   **Figure 3. RIF1 KO causes global alterations of compartments and epigenetic state.**

470   a, Pile up line plots of indicated histone marks at A to B compartment boundary ±1 Mb in WT

471   (black) and RIF1 KO (blue) HCT116 and H9 hESCs. b, Correlation matrices and PC1

472   Eigenvector of Chr4 in WT and RIF1 KO H9 hESCs (top) and HCT116 (bottom). c, Example ICE

473   normalized Hi-C contact map of Chr6 91.6-167.8 Mb in H9 hESC (top) and Chr4 138.75-171.35

474   Mb in HCT116 (bottom) WT and RIF1 KO cells with accompanying PC1 Eigenvector plots.

475   Eigenvector plots are overlaid between contact maps. Below are expanded views of insets 1

476   and 2 with accompanying H3K27ac ChIP-seq plots. Arrows indicate compartments and ChIP-

477   seq peaks that are lost upon RIF1 KO. d, Fold enrichment signal pile ups for H3K27ac centered

478   on AtoB compartment switching regions ±1 Mb in WT and RIF1 KO cells sorted by size. Line

479   plots represent cumulative signal in WT (black) and RIF1 KO (blue) cells. e, Aggregate Hi-C

480   log2(obs/exp) interactions between H3K27ac peaks within AtoB compartment switching regions

481   ±1.2 Mb in WT and RIF1 KO H9 hESCs. f, Genome wide saddle plots in WT and RIF1 KO cells.

482   g, Scatterplot of the RT values for upregulated (red) and downregulated (black) H3K27ac peaks

483   in WT (x axis) and RIF1 KO (y axis) HCT116 cells calculated from high resolution Repli-seq

484   data.

485

486   **Figure 4. RT effects precede compartment changes.**

487   a, Images of HCT116-mAID-mClover nuclei after 24 hrs with DMSO (top) or 500uM Auxin

488   (bottom). b, E/L Repli-seq plots of Chr1 172.6-197.6 Mb in HCT116 RIF1-mAID-mClover cells

489   plus 24hrs DMSO (black), plus 24hrs Auxin (grey) and HCT116 RIF1 KO (blue). c, log2 (E/L) RT

490   probability density plots of HCT116-mAID-mClover cells plus 24hrs DMSO (black), plus 24hrs

491   Auxin (grey) and RIF1 KO (blue) HCT116 cells. d, E/L log2(RT) (top row), PC1 Eigenvector

492   (middle row) and correlation matrices (bottom row) of Chr6 95.5-154 Mb in HCT11-mAID-

493   mClover cells plus 24hrs DMSO (left), plus 24hrs Auxin (middle) and RIF1 KO HCT116 (right).

494   e, Saddle plots showing *cis*-compartmental contacts of HCT11-mAID-mClover cells plus 24hrs

495   DMSO (left) and plus 24hrs Auxin (right) binned into 50 segments of increasing PC1

496   Eigenvector values. f, Ordered Euclidian distance measurements for genome wide RT (left) and

497   genome wide log2(obs/exp) (right) between HCT116 RIF1-mAID-mClover plus 24hrs Auxin and

498   either HCT116 RIF1-mAID-mClover control cells (black) or HCT116 RIF1 KO cells (blue). g,

499   Log2(obs/exp) aggregate interactions between B compartments in HCT116 RIF1-mAID-

500   mClover cells plus 24hrs DMSO (left) and plus 24hrs Auxin (right). The interactions were binned

501   into 11 equal segments ranked by delta H3K9me3 between WT HCT116 and RIF1KO HCT116.

502   h, Aggregate Hi-C log2(obs/exp) interactions ±1.5 Mb between H3K9me3 domains as defined in

503   RIF1 KO HCT116 cells in HCT116 RIF1-mAID-mClover cells plus 24hrs DMSO (left) and plus

504   24hrs Auxin (right). i, Aggregate Hi-C log2(obs/exp) interactions ±1.2 Mb between H3K27ac

505   peaks within AtoB compartment switching regions as defined in RIF1KO HCT116 cells in

506   HCT116 RIF1-mAID-mClover cells plus 24hrs DMSO (left) and plus 24hrs Auxin (right).j, A

507   model figure depicting the role of replication timing in maintaining epigenetic status and

508   compartmentalization. In WT cells temporal segregation of replication contributes to the

509   likelihood of nascent chromatin to the assembled into euchromatin (early replicating) or

510   heterochromatin (late replicating). RIF1 and H3K9me3 maintain this temporal segregation in WT

511   cells and allow for preferential 3D contacts between like chromatin types. In RIF1 KO cells this

512   temporal segregation is majorly disrupted, decreasing the likelihood of nascent chromatin

513   assembly into the correct parental form and disrupting 3D contacts between chromatin.

514

515

516   **Supplementary Materials:**

517

518   **Fig. S1. CRISPR/Cas9 RIF1 KO does not cause cell cycle arrest.**

519   a, RIF1 KO in H9 hESCs was achieved by CRISPR/Cas9 cutting at regions up and down

520   stream of exon 3 in the RIF1 coding sequence. Knock in of an eGFP tag was achieved by

521   CRISPR/Cas9 cutting at a region near the start codon and providing a repair vector containing

522   the eGFP coding sequence and flanking homology arms. RIF1 KO HAP1 cells were purchased

523   from Horizon Discovery (HZGHC000663c010) but had a similar deletion of exon3. b, RIF1 GFP

524   tagging in HCT116 was achieved by CRISPR/Cas9 cutting at regions upstream of exon 2 and

525   downstream of exon 3 and providing a repair vector that contained an eGFP tagged version of

526   exon 2 and a loxP flanked exon 3 as well as a blasticidin resistance gene. Cre expression was

527   then used to remove exon 3. In both cell lines removal of exon 3 caused a premature stop

528   codon to be added to the RIF1 mRNA and thus a nonfunctional, truncated protein produced. c,

529   Immunoblot of RIF1 protein in WT and two KO clones of HCT116 and H9 hESCs. Ponceau S

530   total protein stain shown as loading control. d, 2-dimensional (2D) cell cycle analysis using

531   FACS to detect incorporation of 488 anti BrdU (y axis) and DNA content by propidium iodide (x

532   axis) in WT and RIF1 KO cells. e, Average bar plots of three replicates of 2D FACS analysis for

533   each sample with standard deviation error bars; table of p values by t-test between comparators

534   for each cell line. f, E/L repli-seq plot of chr2 in WT (black) and two clones of RIF1 KO (blue and

535   red) H9 hESC (top). E/L repli-seq plot of chr1 in WT (black) and RIF1 KO (blue) mouse ESCs

536   from (*11*)(bottom).

537

538   **Fig. S2. RIF1 KD in H9 hESCs causes intermediate RT changes with no change to**

539   **genome compartmentalization.**

540   a, Immunoblot of control and RIF1 shRNA in H9 hESCs. b, Repli-seq data of Chr1 172.6-197.6

541   Mb in control shRNA and RIF1 shRNA H9 hESCs. Same region as RIF1 KO in Fig 1a. c,

542   Genome wide probability density of E/L Repli-seq RT values in control and RIF1 shRNA H9

543   hESCs. d, Scatterplot of genome wide PC1 eigenvector values for 250kb bins between RIF1

544   shRNA H9 hESCs (x axis) and control shRNA H9 hESCs (y axis) (top). Scatterplot of genome

545 wide PC1 eigenvector values for 250kb bins between RIF1 KO H9 hESCs (x axis) and WT H9

546 hESCs (y axis) (bottom) e, Region Chr3 148.25-151.75 Mb of E/L RT and PC1 eigenvector in

547 shRNA H9 hESCs and RIF1 KO H9 hESCs. f, Log2(obs/exp) aggregate Hi-C interactions

548 centered on genome wide H3K27ac peaks ±1.2 Mb in control shRNA, RIF1 shRNA, and RIF1

549 KO H9 hESCs.

550

551 **Fig. S3. Replication foci patterns are disrupted in RIF1 KO cells.**

552 a, Example BrdU incorporation patterns of S phase human cells. b, Quantification of percentage

553 of S phase BrdU incorporation patterns in WT and RIF1 KO H9 hESCs and HCT116.

554

555 **Fig. S4. High resolution and single cell Repli-seq reveal major RT heterogeneity in RIF1**

556 **KO cells.**

557 a, High resolution Repli-seq pile up plots in WT and RIF1 KO H9 hESCs and HCT116 centered

558 on IZs timing categories called in WT cells ±750 Kb. b, Log10 fold enrichment qPCR results of

559 BrdU incorporated mouse DNA spike in target over BrdU negative mouse DNA spike in

560 background after BrdU immunoprecipitation of each S phase fraction in WT and RIF1 KO H9

561 hESCs and HCT116 cells to approximate pull-down efficiency. WT and RIF1 KO of both cell

562 lines show consistent and similar pull-down efficiencies. c, High resolution Repli-seq pile ups

563 centered on RT changed regions called in E/L Repli-seq data (top) and RT unchanged regions

564 called in E/L Repli-seq (bottom) in WT and RIF1 KO HCT116 ±750 Kb. d, RT indices calculation

565 method used in e. e, RT indices calculated from high resolution Repli-seq for RT changed

566 regions called in E/L Repli-seq data (top) and RT unchanged regions called in E/L Repli-seq

567 (bottom) in WT and RIF1 KO HCT116. H9 hESCs RT indices not shown because of similarity

568 between all indices in RIF1 KO. Examples H9 hESC RT indices in Fig 2b. f, Genome wide

569 probability density plots of RT changes between WT and KO for each cell line, calculated from

570 high resolution Repli-seq. Dotted lines indicate those regions called as having negative RT_{diff}

571 (green), close-to-zero RT_{diff} (grey), or positive RT_{diff} (red). Table shows percentages of genome

572 within each category. g, Violin plots of genome wide T_{width} of high resolution Repli-seq data in WT

573 and RIF1 KO H9 hESCs and HCT116. h, Boxplot of population-based E/L Repli-seq RT for

574 replicated (red) and unreplicated (grey) bins for each single-cell in both WT (top) and RIF1 KO

575 (bottom) HAP1 ranked between 30 and 70% S-phase progression.

576

577 **Fig. S5. RIF1 and H3K9me3 control late replication via independent mechanisms.**

578   a, Histogram of RIF1 Cut&Run read density versus genome wide RT in H9 hESCs and

579   HCT116. b, Boxplots of size distributions of H3K9me3 peaks or domains in affected and

580   unaffected regions in WT H9 hESCs and HCT116; ***p < 0.0005. c, Scatterplot of H3K9me3

581   peaks in WT (x axis) and RIF1 KO (y axis) cells. Significant peak differences are those with at

582   least 2-fold difference and an FDR < 0.05. Upregulated peaks colored in green and

583   downregulated peaks colored in cyan. d, Immunoblot of H3K9me3 in WT and RIF1 KO H9

584   hESCs at three dilutions. Ponceau S total protein stain shown as loading control. e, Venn

585   Diagrams of shared H3K9me3 domains (left) and unaffected RT regions (right) between RIF1

586   KO HCT116 and H9 hESCs. f, Log2(obs/exp) aggregate Hi-C interactions between H3K9me3

587   peaks genome wide ±1.5 Mb in WT and RIF1 KO HCT116 and H9 hESCs. g, Log2(obs/exp)

588   interactions between H3K9me3 peaks as called in f over genomic distance in WT (black) and

589   RIF1 KO (red) cells. Log2(obs/exp) interactions between upregulated H3K9me3 peaks (left).

590   Log2(obs/exp) interactions between downregulated H3K9me3 peaks (middle). Log2(obs/exp)

591   interactions between upregulated and downregulated H3K9me3 peaks (right). h, Scatterplot of

592   H3K27ac peak RPM in WT (x axis) and RIF1 KO (y axis) cells. Significant peak differences are

593   those with at least 2-fold difference and an FDR < 0.05. Upregulated peaks colored in green (n

594   = 5697 in RIF1 KO H9 hESCs, n = 3646 in RIF1 KO HCT116) and downregulated peaks

595   colored in cyan (n = 61617 in RIF1 KO H9 hESCs, n = 21799 in RIF1 KO HCT116). i,

596   Immunoblot of H3K27ac in WT and RIF1 KO H9 hESCs at three dilutions. Ponceau S total

597   protein stain shown as loading control.

598

599   **Fig. S6. Intra B compartment interactions are strengthened and intra A compartment**

600   **interactions are weakened in RIF1 KO cells.**

601   a, 2-D histogram of PC1 eigenvector values of diffHi-C points of downregulated (left) and

602   upregulated (right) Hi-C interactions in H9 hESCs. b, 2-D histogram of PC1 eigenvector values

603   of diffHi-C points of downregulated (left) and upregulated (right) Hi-C interactions in HCT116

604   cells.

605

606   **Fig. S7. TAD positions are maintained, and boundaries are strengthened in RIF1 KO**

607   **cells.**

608   a, ICE normalized region at Chr2 75.2-85.45 Mb showing a TAD boundary formation at a region

609   of RT and H3K9me3 change in HCT116. WT RIF1 Cut&Run shown for comparison to RT and

610   H3K9me3 ChIP-seq. Black dotted line indicates TAD boundary in WT cells. Green dotted line

611   indicates new TAD boundary in RIF1 KO cells. b, Log2(obs/exp) interaction pile ups centered at

612   WT and RIF1 KO specific TAD boundaries ±1 Mb in WT and RIF1 KO HCT116 (left). RT indices

613   of WT and RIF1 KO specific TAD boundaries in WT and RIF1 KO HCT116 (right). c,

614   Autocorrelation (y-axis) against lag (x-axis) of insulation scores for unaffected and affected

615   regions in HCT116 WT and RIF1KO. Higher autocorrelation indicates more similarity between

616   insulation scores within the region of interest, therefore fewer boundaries where insulation score

617   increases. Lower autocorrelation indicates more dissimilarity, therefore potentially more

618   boundaries. d, Insulation score pile ups centered on all TAD boundaries genome wide ±1 Mb in

619   WT and RIF1 KO H9 hESCs and HCT116. Line plots represent mean scores in WT (black) and

620   RIF1 KO (red). e, Log2(obs/exp) interaction pile ups centered on TAD boundary ±1 Mb in WT

621   and RIF1 KO H9 hESCs and HCT116. f, Log2(obs/exp) interaction pile ups centered on TAD

622   center ±1 Mb in WT and RIF1 KO H9 hESCs and HCT116. g, Boxplots of log2(intra/interTAD

623   interactions) of A compartment TADs (blue) and B compartment TADs (grey) in WT and RIF1

624   KO H9 hESCs and HCT116.

625

626   **Fig. S8. TAD boundary strengthening is not caused by changes in Rad21 binding in RIF1**

627   **KO cells.**

628   a, Scatterplots of Rad21 ChIP-seq peak read counts in WT (x axis) versus RIF1 KO (y axis).

629   Significant up or down regulated peaks are those with at least 2-fold difference and a FDR <

630   0.05. Common peaks colored in black, upregulated peaks colored in green, and downregulated

631   peaks colored in cyan. b, Log2(obs/exp) interaction pile ups centered at Rad21 peaks that are

632   common (top), downregulated (middle), or upregulated (bottom) ±600kb between WT and RIF1

633   KO cells in HCT116 (left) and H9 hESCs (right).

634

635   **Fig. S9. Histone modifications, not RT or compartments, correlate with gene expression**

636   **alterations in RIF1 KO.**

637   a, Volcano plots of gene expression changes upon RIF1 KO in H9 hESC (left) and HCT116

638   (right). Gene expression changes with a corrected p value < 0.1 were called as differential

639   expression events (up-regulated genes: red, down-regulated genes: green, genes with non-

640   significant changes: grey). b, GO analysis dot plot of differentially expressed genes in RIF1 KO

641   H9 hESCs and HCT116 where the sizes of dots are proportional to the number of genes and

642   the color coding indicates the direction of expression change (red = activated, blue =

643   repressed). c, Heat maps of regularized log2(count) – regularized log2(mean) of all genes in WT

644   and two RIF1 KO clones in both cell lines. Top row contains significantly upregulated genes.

645   Middle row contains significantly downregulated genes. Bottom row contains genes with no

646   significant expression change. Genes in all rows are ranked by relative expression in WT cells.

647   Positions of key pluripotency factors (blue text) and histone modification writers (black text) are

648   indicated. d, Scatterplots of upregulated (red) and downregulated (green) gene RT values in WT

649   (x axis) and RIF1 KO (y axis) H9 hESCs and HCT116. e, Scatterplot of upregulated (red) and

650   downregulated (green) gene PC1 eigenvector values in WT (x axis) and RIF1 KO (y axis) H9

651   hESCs and HCT116. f, Box plots of distribution of WT RT values at down (green) and up (red)

652   regulated genes in both cell lines. Each point represents an individual gene. g, Box plots of

653   distribution of WT PC1 eigenvector values at down (green) and up (red) regulated genes in both

654   cell lines. Each point represents an individual gene. h, Fold enrichment pile up line plots of

655   indicated histone modification ±5kb around TSS of either up (right) or down (left) regulated

656   genes in WT (black) and RIF1 KO (blue) H9 hESCs and HCT116. i, Feature importance of

657   random forest regression modelling of histone modification in predicting direction of for gene

658   expression changes in H9 hESCs.

659

660   **Materials and Methods**

661   **Cell lines:** H9 hESCs were grown in feeder free conditions on Geltrex matrix (Thermo Fisher

662   A14133) coated dishes in StemPro (Thermo Fisher A100701) media according to

663   manufacturer's specifications. hESCs were passaged with ReLeSR (StemCell Technologies

664   05872) according to manufacturer's specifications. RIF1 KO H9 lines were established by

665   transfecting two CRISPR/Cas9 plasmids containing separate sgRNAs that would cut upstream

666   and downstream of RIF1 exon 2. Cells were subcloned and screened by PCR for loss of

667   amplification from exon 2. HCT116 cells were grown in McCoy's 5A media plus 10% FBS and

668   1% Pen/Strep. HCT116 lines were established by CRISPR/Cas9 knock in of eGFP-RIF1-FLOX

669   construct and blasticidin selection. Selected cells were dissociated to single cells and diluted to

670   100 cells per 10cm plate and allowed to grow into colonies for 1-2 weeks. Clones with

671   homozygous integration of the eGFP-RIF1-FLOX construct were screened by PCR. RIF1 was

672   deleted from HCT116 eGFP-RIF1-FLOX cell lines by transient transfection with pAAV-Ef1a-

673   mCherry-IRES-Cre (addgene.com Plasmid #55632) and FACS sorting of mCherry positive cells.

674   Positive cells were dissociated to single cells and diluted to 100 cells per 10cm plate and

675   allowed to grow into colonies for 1-2 weeks. Clones with homozygous deletion of RIF1 exon3

676   were screened by PCR. RIF1-mAID-mClover HCT116 cells were established as in (*30*). HAP1

677   WT and RIF1 KO cells were purchased from Horizon Discovery (HZGHC000663c010) and

678   grown in IMDM plus 10% FBS and 1% Pen/Strep according to manufacturer's instructions.

679

680   **RIF1 degradation with AID:** RIF1-mAID-mClover HCT116 cells were incubated with 2ug/mL

681   doxycycline and 100uM Auxinole (*31*) for 24 hrs to induce OsTIR1 expression and suppress its

682   activity. Auxinole was washed away and fresh media plus 2ug/mL doxycycline plus 500 uM IAA

683   (Sigma I2886) was added for 24hrs to degrade RIF1. Control cells remained in doxycycline and

684   Auxinole for an additional 24hrs. RIF1 degradation was confirmed by microscopy and western

685   blotting.

686

687   **2 fraction RT profiling and analysis:** Genome-wide RT profiles were generated as previously

688   described (*12*) with the following modifications: RT datasets were not normalized by quantile

689   normalization since this processing step will result in the enforcement of WT distribution on KO,

690   thereby preventing the detection of any genome-wide RT changes. The Loess smoothed

691   coverages are scaled using robust scaler from the python package scikit-learn (http://scikit-

692   learn.org) instead. The scaler removes median and scales the datasets to their collective inter-

693   quantile range according to:

694

695   **xscaled=(x-median(x))/x.quantile(0.75)-x.quantile(0.25)**

696

697   (equation I)

698

699 As a result, different datasets with varying dynamic ranges directly comparable to each other.

700 Sex chromosomes were excluded from Repli-seq analysis.

701

702   **Replication foci staining:** Asynchronous cells were grown on coverslips until 70% confluence

703   and pulsed with BrdU for 30 minutes. Cells were then washed with PBS and fixed in cold 70%

704   EtOH. Chromatin was denatured with 1.5 N HCl 30min RT and washed away. Cells were

705   permeabilized with PBS plus 0.5% Tween20 for 5min RT. Mouse anti-BrdU (BD 55567) (1:50) in

706   PBS plus 10% goat serum was added for 1hr at RT and washed away. Goat 488 anti-mouse

707   (1:100) in PBS plus 10% goat serum was added for 1hr at RT and washed away. Nuclei were

708   stained with DAP1 and cells were imaged on the DeltaVision (GE Life Sciences) microscope.

709   Patterns were categorized as early, middle, late, or blended as in Extended Data Fig 3a.

710

711   **High resolution RT profiling and analysis:** High resolution Repli-seq was performed and

712   analyzed as previously described (*14*). Briefly, asynchronously growing cells were labeled with

713   BrdU (400 uM) for 30 minutes followed by ethanol fixation. PI staining for DNA content was

714 carried out and 16 fractions of S phase were sorted on the FACS. Gates were set by marking

715 G1 and G2 peaks and dividing S phase into 16 equal fractions between the peaks. At least 80k

716 cells were sorted for each S phase fraction. BrdU incorporated mouse mitochondrial DNA and

717 BrdU negative mouse DNA was spiked into the purified genomic DNA to serve as a BrdU

718 immunoprecipitation control. BrdU incorporated DNA was immunoprecipitated using mouse anti-

719 BrdU (BD 55567). Libraries were prepared for Illumina sequencing with NEBNext Ultra DNA

720 Library Prep Kit for Illumina (E7370). The reads were aligned to hg38 using bowtie2 with

721 parameters --no-mixed --no-discordant --reorder. Replication heatmap matrices were

722 constructed from RPM (read per million) bedgraph files at 50kb window size ranked from S1 to

723 S16. The matrices were Gaussian smoothed with lambda=1 and column-wise scaled. Sex

724 chromosomes were excluded from the heatmap matrix construction.

725

726 **Calculating RT indices from high resolution Repli-seq:** For each 50kb genomic bin the RT

727 indices computed according to the equation below and graphically illustrated in Supplementary

728 Figure 4b:

729 **RTindex=log2(Sum(S1*8,S2*7,S3*6,...S8*1)/Sum(S9*1,S10*2,S11*3...S16*8))**

730   (equation II)

731 RT_{diff} is computed by subtracting $RTindex_{KO}$ from $RTindex_{WT}$.

732 **Calling unaffected and affected regions using high resolution Repli-seq:** We fitted a

733 Gaussian Mixture model probability distribution on RT_{diff} between WT and KO calculated for all

734 genomic bins. The model is composed of three distribution components: one that contains large

735 negative values representing the bins that on a population level replicate later in WT and earlier

736 in KO, a second distribution of positive values representing bins that on a population level

737 replicate earlier in WT and later in KO, a third one that contains values close to zero

738 representing the bins that on a population level replicate at times statistically indistinguishable

739 from WT. The validity of the model is checked through the minimization of Bayesian information

740 criterion. Continuous 50kb genomic bins that were associated with negative RT indices in WT

741 and assigned to the first distribution were called as affected late regions. Continuous 50kb

742   genomic bins that were associated with negative RT indices in WT but assigned to the third

743   distribution were called as unaffected late regions.

744   **T_{width} from high resolution Repli-seq:** The degree of heterogeneity of RT was estimated by

745   performing a sigmoidal fitting on the column wise cumulative replication percentage as

746   previously described (*14*). Briefly, the sigmoidal function below:

$$f(x) = \frac{e^{-kx}}{1 + e^{-kx}}$$

747

748   (equation III)

749

750   was fitted to bin-wise cumulative replication percentage using curve_fit function in scipy, which

751   aims to minimize the mean squared error. Tolerance is set at 0.0001. T_{rep} used in the timing-

752   variation measurement is f(x) when x = 0.5 which means the genomic bin is 50% replicated in

753   the cell population and T_{width} used in the timing-variation measurement is f(0.75) – f(0.25) which is

754   the time difference between 75% replicated and 25% replicated for any genomic bin.

755

756   **Single cell Repli-seq:** Single cell RT was performed as previously described (*15*) with slight

757   modifications. Briefly, single cells were sorted from five evenly spaced windows throughout S

758   phase directly into individual wells of a 96 well plate containing single cell lysis buffer and lysed

759   at 50°C for 1 hour followed by 4 minutes at 99°C. Whole genome amplification (WGA) was

760   performed as previously described (*32*) and unique barcodes were added to each individual

761   WGA product followed by purification and pooling for NEBNext Ultra DNA Library preparation.

762

763   **Single cell Repli-seq analysis**: Single cell Repli-seq fastqs were first demultiplexed according

764   to the barcodes added during library making using custom script. The reads were trimmed

765   100bp from the 5' end using CutAdapt (https://github.com/marcelm/cutadapt) and subsequently

766   aligned to hg38 using bowtie2 with the parameters --no-mixed --no-discordant --reorder. Cells

767   with fewer than 250,000 reads aligned were filtered out. Subsequent analysis was carried out as

768   previously described (*15*). Briefly, mappability correction using G1 cells and smoothing were

769   applied to RPM was calculated in 50kb bins for single cells. Binarization was subsequently

770   carried out on smoothed RPM signal files by applying a 2-component mixed Gaussian model

771   where bins assigned to the distribution with lower mean RPM were binarized to 0 (unreplicated)

772   and those that were assigned to the distribution with higher mean RPM were binarized to 1

773   (replicated). Heatmaps were generated by sorting according to copy number with the cell with

774   the fewest bins replicated at the top and that with the most bins replicated at the bottom. T_{width}

775   calculation was performed as previously described (*15*). Briefly, for individual bins, an index

776   called 'time from population average replication' was calculated, which represents the time in

777   hours passed from the time of replication indicated from E/L repli-seq. A negative number

778   indicates that according to E/L repli-seq the genomic bin should not have undergone replication

779   on a population level whereas a positive number indicates that according to E/L repli-seq the bin

780   should have finished replicating. The 2-D distributions of such indices against % replicated were

781   plotted as heatmaps. A sigmoidal curve was fitted to the distribution as described above in

782   'Twidth from high resolution Repli-Seq'.

783

784   **ChIP-seq experiments and analyses:** ChIP-seq experiments in HCT116 cells and H9 hESCs

785   were carried out as previously described (*33*). After removal of medium, cells were crosslinked

786   in 1% formaldehyde in PBS at room temperature for 10 min and quenched with glycine. PBS

787   rinsed cell pellets were flash frozen in liquid nitrogen and stored at -80°C or continue with cell

788   and nuclear lysis steps. Nuclear lysates were precleared with protein A/G beads followed by

789   incubation with proper antibodies. After washing with high salt buffer, LiCl buffer, and TE,

790   chromatin was eluted and reverse crosslinked. Purified DNA was ethanol precipitated followed

791   by Illumina Truseq library preparation. Libraries for Illumina sequencing were constructed using

792   the following standard protocol. Fragment ends were repaired using the NEBNext End Repair

793   Module and adenosine was added at the 3' ends of fragments using Klenow fragment (3' to 5'

794   exo minus, New England Biolabs), universal adaptors were ligated to the A-tailed DNA

795   fragments at room temperature for 1 h with T4 DNA ligase (New England Biolabs) and amplified

796   with Illumina barcoded primers using KAPA SYBR FAST qPCR Master Mix for 5~12 PCR cycles

797   to obtain enough DNA for sequencing. Generated libraries were paired-end sequenced on

798   Illumina HiSeq2500 v4. ChIP-seq datasets were aligned to hg38 using bowtie-2 with the

799   parameters --no-mixed --no-discordant --reorder. Resulting bam files for each histone mark

800   were sorted and deduplicated using samtools. Deduplicated bam tools for ChIPed and input

801   libraries were passed onto the peak calling algorithm MACS2 for peak calling and generating

802   fold enrichment signal tracks. The heatmaps centered at features were constructed by filling a

803 matrix where the rows represent individual ChIP-seq fold enrichment signals around individual

804 features.

805

806 **RIF1 Cut&Run:** Cut&Run was performed as previously described (*16*) with antibody against

807 eGFP in eGFP-RIF1 tagged H9 hESCs and HCT116. Briefly, cells were washed and bound to

808 Concanavalin-A-coated magnetic beads, and permeabilized in wash buffer (20 mM HEPES pH

809 7.5, 150 mM NaCl, 0.5 mM spermidine and one Roche Complete protein inhibitor tablet per 50

810 mL) containing 0.03% digitonin and 20 mM EDTA (Dig-wash). Antibody was added to a final

811 concentration of 1:100 and incubated overnight at 4°C. Cells were washed with Dig-wash buffer

812 and incubated with Protein-A-MNase (pA-MN) for 1 hour at 4°C. Cells were washed three times

813 with Dig-wash buffer to remove unbound pA-MN before placing cells in an ice-cold block and

814 activating cleavage with the addition of CaCl2 to 2mM final concentration. Cleavage was

815 stopped by the addition of 2x Stop Buffer (340 mM NaCl, 20 mM EDTA, 4 mM EGTA, 0.05%

816 Digitonin, 0.05 mg/mL glycogen, 5 µg/mL RNase A), and fragments were released by 30 min

817 incubation at 37°C. Supernatant was recovered and DNA was purified with phenol:chloroform

818 extraction and precipitation with ethanol, before being used as input for library preparation.

819

820 **Calling H3K9me3 domains**: In addition to applying MACS2 (*34*) and epic2 (*35*) on H3K9me3

821 ChIP-seq datasets to call peaks, we also called large H3K9me3 domain. H3K9me3 fold

822 enrichment was calculated as a log2 ratio over input in 50kb genomic bins. Considering any

823 genomic bin can assume one of two states: inside or outside of a H3K9me3 domain, a two-state

824 hidden markov model was fitted to the fold enrichment distribution with tolerance set at 0.0001.

825 Implementation was carried out in Python using the hmmlearn package

826 (https://github.com/hmmlearn/hmmlearn). Each genomic bin was assigned a state using the

827 Viterbi algorithm. The state associated with the higher signal mean was inside H3K9me3

828 domain. H3K9me3 domain was therefore defined as continuous genomic bins associated with

829 the state of higher mean signal.

830

831 **Hi-C procedure and sequence processing**: Two subclones of H9 and HCT116 RIF1 KO cells

832 were prepared and processed for Hi-C as previously described (*36*) using DpnII for digestion.

833 ~1 billion 50bp paired-end reads were obtained for each subclone for both H9 and HCT116.

834 Reads were processed using HiCUP pipeline available from Babraham Institute

835 (https://www.bioinformatics.babraham.ac.uk). Briefly the reads were truncated at DpnII

836 recognition sites and mapped to hg38 using bowtie2. The uniquely mapped reads were further

837   filtered to remove common Hi-C artefacts e.g. self-ligated fragments and same frag and

838   subsequently deduplicated. Bam files were converted to cooler files using 4DN DCIC utility

839   bam2pairs and cooler load at 5kb, 50kb, 100kb and 250kb. Hi-C maps used in this work were

840   either normalized using iterative correction (ICE) (*37*) or distance normalized as log2

841   (observed/expected) where expected is computed according to the equation below:

842

$$\frac{\sum_{i}^{j} diagonal(|i - j|)}{(|i - j|)}$$

843

844   (Equation IV)

845

846   Eigendecomposition is performed using cooltools package and eigenvectors are ranked using

847   gene density.

848

849   **TAD calling**: TADs and insulating boundaries in this work were called using DI (*22*) and

850   insulation score (*38*) respectively at 50kb bins with a sliding window of 1Mb.

851

852   **Calling differential interacting pairs**: Differential interacting pairs were called using diffHiC

853   (*21*). Briefly, read counts matrices were generated from bam files resulting from HiCUP for WT

854   and RIF1 KO. Subsequently, edgeR (*39*) was applied to count matrices to estimate technical

855   noise between replicates and call differential pairs by quasi-F test through generalized linear

856   model (glm) fitting. Pairs with >=2-fold difference and <0.05 FDR were called to be up- or down-

857   regulated depending on the sign of fold change.

858

859   **RNA-seq:** Libraries were prepared with NEBNEXT rRNA Depletion kit (human/mouse/rat) and

860   NEBNEXT Ultra II Directional RNA Library Prep kit for Illumina (New England Biolabs)

861   according to manufacturer's instructions. Sample input was 900ng total RNA (determined by

862   Qubit RNA HS reagents, Thermo) with a RIN >8 (TapeStation High Sensitivity RNA ScreenTape

863   Assay, Agilent). RNA was fragmented for 15 minutes and libraries were constructed with a 1/5th

864   dilution of NEB adaptor and 12 cycles of PCR amplification with dual-indexing primers.

865   Amplified libraries were initially quantified by Qubit DNA HS reagents and checked for size and

866   artifacts using TapeStation DNA HS reagents. Excess adaptors were removed using an

867   additional 0.9x AMPure bead purification. KAPA qPCR (KAPA Biosystems) was used to

868   determine molar quantities of each library and individual libraries were diluted and pooled at

869   equimolar concentrations. The final library pool was again checked by TapeStation and KAPA

870   qPCR before submission for sequencing. Fastq reads were aligned to hg38 using STAR aligner

871   with the options --quantMode GeneCounts and --bamRemoveDuplicatesType UniqueIdentical

872   turned on. Gene count files were generated using HTseq (https://github.com/simon-

873   anders/htseq)   from   bam   files   produced   by   STAR   aligner.   DEseq2

874   (https://bioconductor.org/packages/release/bioc/html/DESeq2.html) was subsequently used to

875   call differentially expressed transcripts using gene count files as input.

876

877   **Random Forest Classifier:** Random forest classification for differentially expressed genes was

878   performed on arrays where each row represented the TSS of a differentially expressed gene

879   and each column represented the RPM signal of H3K27ac, H3K4me3, H3K27me3 and

880   H3K9me3 according to the algorithm presented in (*40*) using scikit-learn.

881

882   Reference:

883   1.   N. Rhind, D. M. Gilbert, DNA Replication Timing. *Cold Spring Harb. Perspect. Biol.* **5**,

884   a010132 (2013).

885   2.   C. Marchal, J. Sima, D. M. Gilbert, Control of DNA replication timing in the 3D genome.

886   *Nat. Rev. Mol. Cell Biol.* (2019), , doi:10.1038/s41580-019-0162-y.

887   3.   N. Reverón-Gómez, C. González-Aguilera, K. R. Stewart-Morgan, N. Petryk, V. Flury, S.

888   Graziano, J. V. Johansen, J. S. Jakobsen, C. Alabert, A. Groth, Accurate Recycling of

889   Parental Histones Reproduces the Histone Modification Landscape during DNA

890   Replication. *Mol. Cell* (2018), doi:10.1016/j.molcel.2018.08.010.

891   4.   T. M. Escobar, O. Oksuz, R. Saldaña-Meyer, N. Descostes, R. Bonasio, D. Reinberg,

892   Active and Repressed Chromatin Domains Exhibit Distinct Nucleosome Segregation

893   during DNA Replication. *Cell* (2019), doi:10.1016/j.cell.2019.10.009.

894   5.   L. Lande-Diner, J. Zhang, H. Cedar, Shifts in Replication Timing Actively Affect Histone

895   Acetylation during Nucleosome Reassembly. *Mol. Cell.* **34**, 767–74 (2009).

896   6.   M. Hayano, Y. Kanoh, S. Matsumoto, C. Renard-Guillet, K. Shirahige, H. Masai, Rif1 is a

897   global regulator of timing of replication origin firing in fission yeast. *Genes Dev.* **26**, 137–

898   150 (2012).

899   7.   J. M. Peace, A. Ter-Zakarian, O. M. Aparicio, Rif1 regulates initiation timing of late

900   replication origins throughout the S. cerevisiae genome. *PLoS One.* **9** (2014),
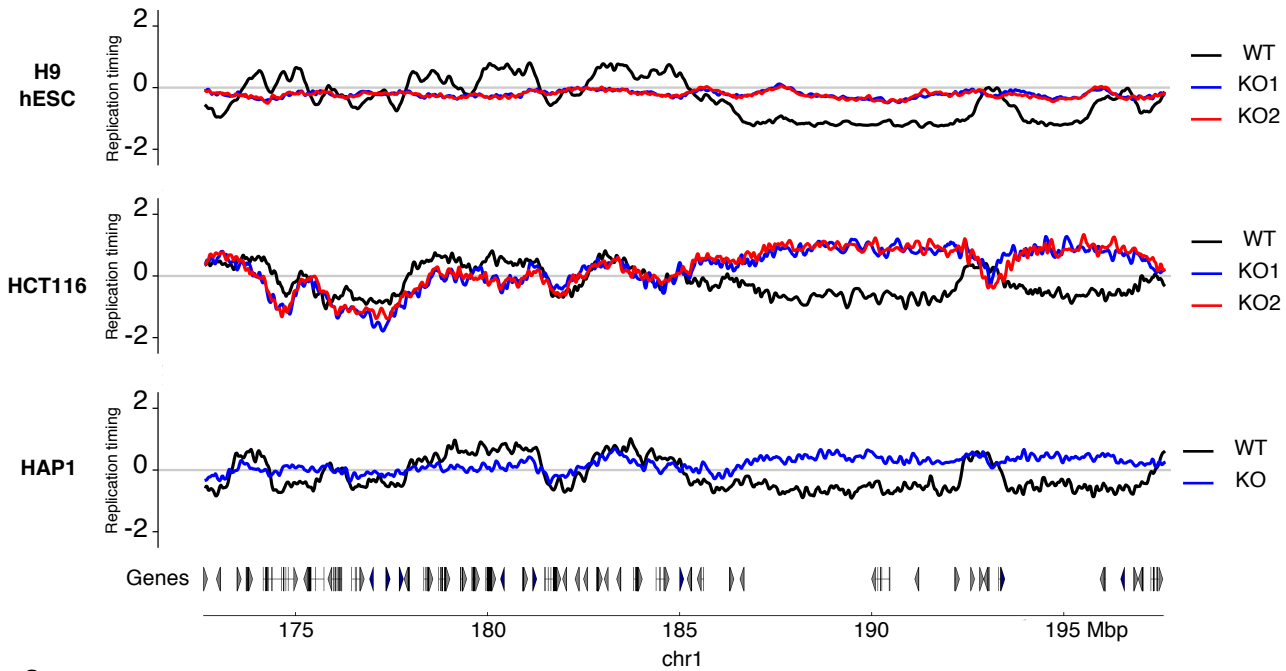
901   doi:10.1371/journal.pone.0098501.

902   8.   D. Cornacchia, V. Dileep, J.-P. P. Quivy, R. Foti, F. Tili, R. Santarella-Mellwig, C. Antony,
903   G. G. Almouzni, D. M. Gilbert, S. B. C. C. Buonomo, Mouse Rif1 is a key regulator of the
904   replication-timing programme in mammalian cells. *EMBO J.* **31**, 3678–3690 (2012).
905   9.   S. Yamazaki, A. Ishii, Y. Kanoh, M. Oda, Y. Nishito, H. Masai, Rif1 regulates the
906   replication timing domains on the human genome. *EMBO J.* **31**, 3667–3677 (2012).
907   10.   E. Sreesankar, V. Bharathi, R. K. Mishra, K. Mishra, Drosophila Rif1 is an essential gene
908   and controls late developmental events by direct interaction with PP1-87B. *Sci. Rep.* **5**,
909   10679 (2015).
910   11.   R. Foti, S. Gnan, D. Cornacchia, V. Dileep, A. Bulut-Karslioglu, S. Diehl, A. Buness, F. A.
911   A. Klein, W. Huber, E. Johnstone, R. Loos, P. Bertone, D. M. M. Gilbert, T. Manke, T.
912   Jenuwein, S. C. B. C. B. B. Buonomo, Nuclear Architecture Organized by Rif1 Underpins
913   the Replication-Timing Program. *Mol. Cell.* **61**, 260–273 (2016).
914   12.   C. Marchal, T. Sasaki, D. Vera, K. Wilson, J. Sima, J. C. Rivera-Mulia, C. Trevilla-García,
915   C. Nogues, E. Nafie, D. M. Gilbert, Genome-wide analysis of replication timing by next-
916   generation sequencing with E/L Repli-seq. *Nat. Protoc.* **13**, 819–839 (2018).
917   13.   R. T. O'Keefe, S. C. Henderson, D. L. Spector, Dynamic organization of DNA replication
918   in mammalian cell nuclei: spatially and temporally defined replication of chromosome-
919   specific alpha-satellite DNA sequences. *J. Cell Biol.* **116**, 1095–1110 (1992).
920   14.   P. A. Zhao, T. Sasaki, D. M. Gilbert, High Resolution Mapping of the Temporal
921   Replication Landscape of the Human and Mouse Genome. *bioRxiv*, 755629 (2019).
922   15.   V. Dileep, D. M. Gilbert, Single-cell replication profiling to measure stochastic variation in
923   mammalian replication timing. *Nat. Commun.* **9**, 427 (2018).
924   16.   P. J. Skene, S. Henikoff, An efficient targeted nuclease strategy for high-resolution
925   mapping of DNA binding sites. *Elife* (2017), doi:10.7554/elife.21856.
926   17.   D. Nicetto, K. S. Zaret, Role of H3K9me3 heterochromatin in cell identity establishment
927   and maintenance. *Curr. Opin. Genet. Dev.* **55**, 1–10 (2019).
928   18.   T. Ryba, I. Hiratani, J. Lu, M. Itoh, M. Kulik, J. Zhang, T. C. Schulz, A. J. Robins, S.
929   Dalton, D. M. Gilbert, Evolutionarily conserved replication timing profiles predict long-
930   range chromatin interactions and distinguish closely related cell types. *Genome Res.* **20**,
931   761–770 (2010).
932   19.   E. Yaffe, S. Farkash-Amar, A. Polten, Z. Yakhini, A. Tanay, I. Simon, Comparative
933   analysis of DNA replication timing reveals conserved large-scale chromosomal
934   architecture. *PLoS Genet.* **6**, 1–12 (2010).
935   20.   E. Lieberman-Aiden, N. L. Van Berkum, L. Williams, M. Imakaev, T. Ragoczy, A. Telling,

936   I. Amit, B. R. Lajoie, P. J. Sabo, M. O. Dorschner, R. Sandstrom, B. Bernstein, M. A.
937   Bender, M. Groudine, A. Gnirke, J. Stamatoyannopoulos, L. A. Mirny, E. S. Lander, J.
938   Dekker, Comprehensive mapping of long-range interactions reveals folding principles of
939   the human genome. *Science (80-.).* (2009), doi:10.1126/science.1181369.

940 21.   A. T. L. Lun, G. K. Smyth, diffHic: A Bioconductor package to detect differential genomic
941   interactions in Hi-C data. *BMC Bioinformatics* (2015), doi:10.1186/s12859-015-0683-0.

942 22.   J. R. Dixon, S. Selvaraj, F. Yue, A. Kim, Y. Li, Y. Shen, M. Hu, J. S. Liu, B. Ren,
943   Topological domains in mammalian genomes identified by analysis of chromatin
944   interactions. *Nature.* **485**, 376–380 (2012).

945 23.   J. Sima, A. Chakraborty, V. Dileep, M. Michalski, K. N. Klein, N. P. Holcomb, J. L. Turner,
946   M. T. Paulsen, J. C. Rivera-Mulia, C. Trevilla-Garcia, D. A. Bartlett, P. A. Zhao, B. K.
947   Washburn, E. P. Nora, K. Kraft, S. Mundlos, B. G. Bruneau, M. Ljungman, P. Fraser, F.
948   Ay, D. M. Gilbert, Identifying cis Elements for Spatiotemporal Control of Mammalian DNA
949   Replication. *Cell.* **176**, 816–830 (2019).

950 24.   P. Oldach, C. A. Nieduszynski, Cohesin-Mediated Genome Architecture Does Not Define
951   DNA Replication Timing Domains. *Genes (Basel).* **10**, 196 (2019).

952 25.   M. Cremer, K. Brandstetter, A. Maiser, S. S. P. Rao, V. Schmid, N. Mitra, S. Mamberti,
953   K.-N. Klein, D. M. Gilbert, H. Leonhardt, M. C. Cardoso, E. L. Aiden, H. Harz, T. Cremer,
954   Cohesin depleted cells pass through mitosis and reconstitute a functional nuclear
955   architecture. *bioRxiv*, 816611 (2019).

956 26.   A. Burton, M. E. Torres-Padilla, Epigenetic reprogramming and development: A unique
957   heterochromatin organization in the preimplantation mouse embryo. *Brief. Funct.*
958   *Genomics* (2010), doi:10.1093/bfgp/elq027.

959 27.   R. Strauss, P. Hamerlik, A. Lieber, J. Bartek, Regulation of stem cell plasticity:
960   Mechanisms and relevance to tissue biology and cancer. *Mol. Ther.* (2012), ,
961   doi:10.1038/mt.2012.2.

962 28.   K. Nishimura, T. Fukagawa, H. Takisawa, T. Kakimoto, M. Kanemaki, An auxin-based
963   degron system for the rapid depletion of proteins in nonplant cells. *Nat. Methods.* **6**, 917–
964   922 (2009).

965 29.   S. B. C. Buonomo, Y. Wu, D. Ferguson, T. de Lange, Mammalian Rif1 contributes to
966   replication stress survival and homology-directed repair. *J. Cell Biol.* **187**, 385–98 (2009).

967 30.   L. P. Watts, T. Natsume, Y. Saito, J. Garzón, M. T. Kanemaki, S. Hiraga, A. D.
968   Donaldson, The RIF1-Long splice variant promotes G1 phase 53BP1 nuclear bodies to
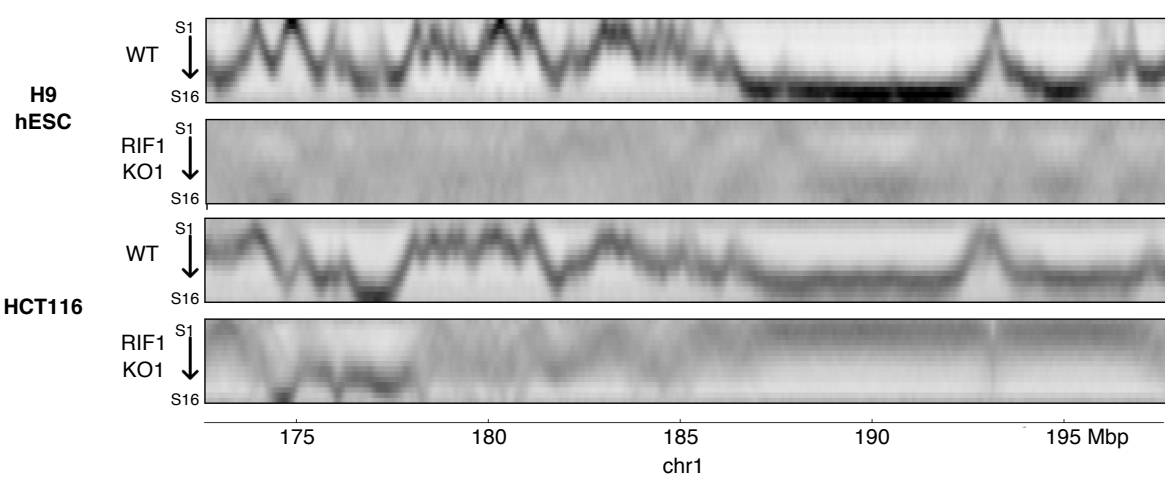969   protect against replication stress. *bioRxiv*, 859199 (2019).

970   31.   A. Yesbolatova, T. Natsume, K. ichiro Hayashi, M. T. Kanemaki, Generation of
971   conditional auxin-inducible degron (AID) cells and tight control of degron-fused proteins
972   using the degradation inhibitor auxinole. *Methods.* **164**–**165**, 73–80 (2019).

973   32.   T. Baslan, J. Kendall, L. Rodgers, H. Cox, M. Riggs, A. Stepansky, J. Troge, K. Ravi, D.
974   Esposito, B. Lakshmi, M. Wigler, N. Navin, J. Hicks, Genome-wide copy number analysis
975   of single cells. *Nat. Protoc.* **7**, 1024–1041 (2012).

976   33.   X. Lyu, M. J. Rowley, V. G. Corces, Architectural Proteins and Pluripotency Factors
977   Cooperate to Orchestrate the Transcriptional Response of hESCs to Temperature Stress.
978   *Mol. Cell.* **71**, 940-955.e7 (2018).

979   34.   Y. Zhang, T. Liu, C. A. Meyer, J. Eeckhoute, D. S. Johnson, B. E. Bernstein, C.
980   Nussbaum, R. M. Myers, M. Brown, W. Li, X. S. Shirley, Model-based analysis of ChIP-
981   Seq (MACS). *Genome Biol.* (2008), doi:10.1186/gb-2008-9-9-r137.

982   35.   E. B. Stovner, P. Sætrom, epic2 efficiently finds diffuse domains in ChIP-seq data.
983   *Bioinformatics* (2019), doi:10.1093/bioinformatics/btz232.

984   36.   S. S. P. Rao, M. H. Huntley, N. C. Durand, E. K. Stamenova, I. D. Bochkov, J. T.
985   Robinson, A. L. Sanborn, I. Machol, A. D. Omer, E. S. Lander, E. L. L. Aiden, A 3D map
986   of the human genome at kilobase resolution reveals principles of chromatin looping. *Cell.*
987   **159**, 1665–1680 (2014).

988   37.   M. Imakaev, G. Fudenberg, R. P. McCord, N. Naumova, A. Goloborodko, B. R. Lajoie, J.
989   Dekker, L. A. Mirny, Iterative correction of Hi-C data reveals hallmarks of chromosome
990   organization. *Nat. Methods* (2012), doi:10.1038/nmeth.2148.

991   38.   B. R. Lajoie, J. Dekker, N. Kaplan, The Hitchhiker's guide to Hi-C analysis: Practical
992   guidelines. *Methods* (2015), doi:10.1016/j.ymeth.2014.10.031.

993   39.   M. D. Robinson, D. J. McCarthy, G. K. Smyth, edgeR: A Bioconductor package for
994   differential expression analysis of digital gene expression data. *Bioinformatics* (2009),
995   doi:10.1093/bioinformatics/btp616.

996   40.   L. Breiman, Random forests. *Mach. Learn.* **45**, 5–32 (2001).
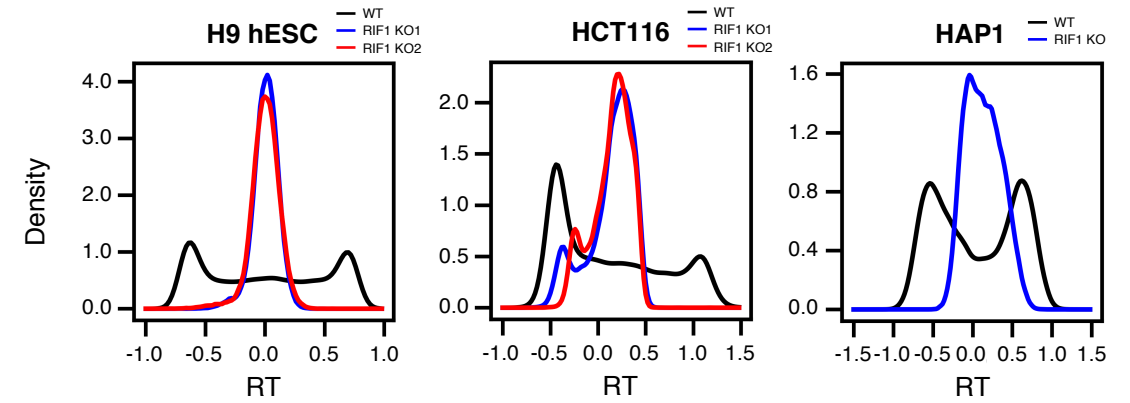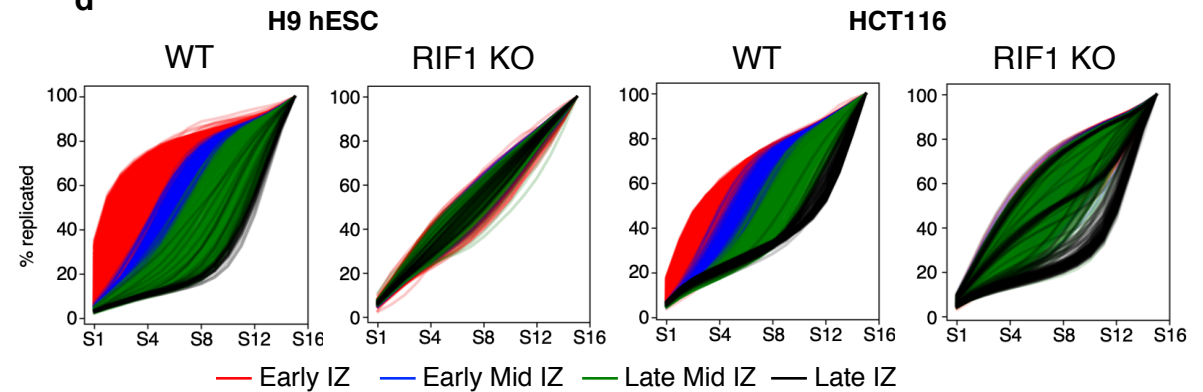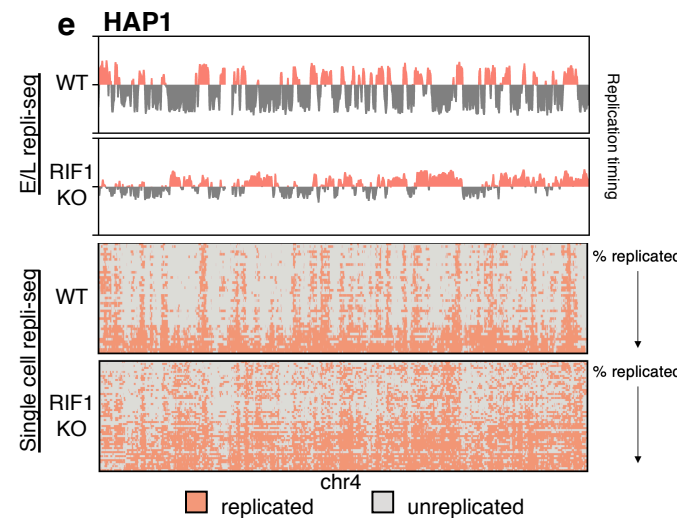
997

998

Figure 1
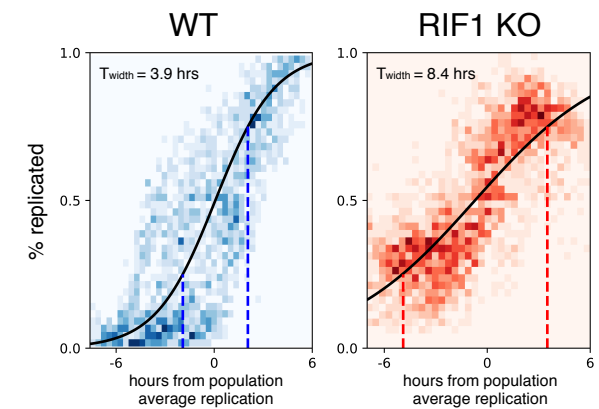
Figure 2

Figure 3

Figure 4